Numerical assessment of human EMF exposure to collocated and distributed massive MIMO deployments in an industrial indoor environment

Sergei Shikhantsov, Arno Thielens, *Member, IEEE,* Günter Vermeeren, *Member, IEEE,*
Piet Demeester, *Fellow, IEEE,* Luc Martens, *Member, IEEE,* and Wout Joseph, *Senior Member, IEEE*

***Abstract*—This article presents a comparative numerical study of the collocated and distributed massive MIMO deployments at 3.5 GHz in an industrial indoor environment from the point of view of the downlink human Electromagnetic field (EMF) exposure. A collection of environmental models incorporating stochastic geometry elements is generated, in which the EMF propagation is calculated using the Ray-Tracing (RT) method. To evaluate the human exposure, the Finite-Difference Time-Domain (FDTD) method is used, including a realistic human phantom and the user equipment model, into which the excitation is introduced based on the RT results. Single-user Maximum Ratio Transmission and multi-user Zero-Forcing scenarios are studied. Small-scale EMF distributions in proximity of the phantom's head are assessed in FDTD and analysed for different user locations in the environment and the user equipment placement with respect to the head. The massive MIMO hot-spot is characterized in terms of its size, instantaneous and time-averaged EMF enhancement, position with respect to the head and the user equipment. The human exposure is assessed using the peak-spatial Specific Absorption Rate averaged over 10 g, referenced to the hot-spot EMF and compared to international guidelines. It is shown that the distributed deployment results in a more accurate and consistent EMF hot-spot around the user equipment with a higher average E-field gain, compared to the collocated deployment. In addition, the distributed configuration produced more compact hot-spots relative to the collocated one, leading to a more than 10-fold average exposure reduction in a multi-user scenario.**

***Index Terms*—5G, 6G, radio access networks, distributed massive MIMO, Ray-Tracing, FDTD, EMF-exposure**

I. Introduction

ONE important feature shared by many visions of the fifth generation (5G) wireless system evolution is a very large number of the base station (BS) antenna elements serving a relatively small number of user equipment (UE) devices [1]. As of the latest release of the 3rd Generation Partnership Project (3GPP), it is planned to augment the existing cellular cites with large array 5G New Radio (5G-NR) BSs [2]. Massive Multiple-Input Multiple-Output (MIMO) is a large antenna array technology that uses the real-time knowledge of the channel state (CS) to configure (*precode*) its transmission to the target UEs. It was first predicted theoretically, and then shown in field trials that such approach delivers record spectral efficiency and sum data rates [3]. Time-Division Duplex (TDD) was used for simultaneous full bandwidth utilization by all served UEs, which transmitted pilot signals in uplink (UL) for the massive MIMO BS to dynamically estimate their CS and set the transmission according to it. *Favorable propagation conditions*, resulting from e.g., rich multipath propagation, are assumed and relied upon to multiplex UEs with no need for computationally-intensive interference cancellation techniques. Under these assumptions, a massive number of BS antennas transmits to multiple UEs through uncorrelated spatially separated streams.

However, it was shown that in some cases, e.g., strong line-of-sight (LOS) components in channels of closely-spaced UEs, favorable propagation does not occur [4], [5], if the BS is sufficiently compact in size. In addition, intra- and inter-cell channel correlation of the UEs that share pilot signals, causes *pilot contamination* [6] which hinders the system performance, and eventually limits the theoretically achievable data rates [7].

Several architectural improvements to massive MIMO were proposed to solve these problems. In Distributed massive MIMO [8], [9] (DMaMIMO), a distributed collection of neighboring remote radio nodes cooperatively and coherently serves the receiver nodes in an opportunistic manner. The radio nodes dynamically form arrays to optimize their beam-forming capacity. A similar concept of cell-free massive MIMO was independently proposed in [10], [11]. It was shown theoretically that access points (APs) spread out randomly in the environment and transmitting coherently deliver an almost 20 times higher per-user throughput compared to a 'small-cell' system in which UEs are connected only to a single AP. Radio Stripes - a conceptual hardware implementation enabling massive distributed antenna systems was presented and discussed in [12], [13].

These concepts, are unified in [14] under the Extremely Large Aperture Arrays (ELAA) paradigm. The ELAA encompasses any massive antenna array (structured or unstructured) distributed over a much larger area, compared to the size of a traditional BS, e.g., a building facade outdoors or a ceiling surface indoors. The large physical size of such arrays increases their spatial focusing resolution, compared to a compact array with equal antenna element count, and effectively puts served UEs in its near field region, if the entire array is treated as one electrically coherent structure.

This common feature of distributed networks is also ex-

S. Shikhantsov, A. Thielens, G. Vermeeren, P. Demeester, L. Martens, G. Torfs and W. Joseph are with Ghent University/IMEC, Department of Information Technology.

pected to have an immense impact on the interaction of the user's body with the electromagnetic field (EMF) radiated in the downlink (DL). In scenarios involving a collocated BS, signals reaching a UE in the far field region often have a dominant direction of arrival (DoA), determined by the relative location of the BS. This may result in the UE being largely shadowed by the user body from the incident EMF. In such situations, the BS array capable of dynamically adjusting its transmission, is either forced to utilize the reflected paths in the environment, or to increase its transmit power to ensure a sufficient signal-to-noise ratio (SNR). The latter inevitably leads to the increase of the EMF power dissipated in the user body blocking the UE device.

A distributed massive MIMO system has higher chance of having multiple unobstructed paths to diverse scenarios of user-UE relative placement, allowing for a more optimal resource allocation in the DL inducing lower exposure of the users. This contribution, for the first time to the authors' best knowledge, presents a numerical study of the human EMF exposure to the DL transmission of a distributed massive antenna array BS. Exposure to 5G systems in the UL is out of scope of this study, and relevant information on this type of exposure can be found in, e.g., [15], [16]. The propagation is modeled with the Ray-Tracing (RT) method in an indoor industrial environment model and the resulting EMF incidence is used to evaluate the exposure of a realistic human phantom with the Finite-Difference Time-Domain (FDTD). Scenarios with distributed and collocated BSs are directly compared in cases with and without the UE device blockage by the phantom's head. The reported insights are valuable for exposure-aware next generation wireless network planning, and for the optimization and standardization of the experimental exposure assessment procedures in such networks.

II. Methods

A. Ray-Tracing

The wireless propagation modeling was performed using a ray-launching [17] variant of the general RT method [18] using REMCOM Wireless InSite 3.3 [19]. The RT method was shown to accurately reproduce the correlation properties of massive MIMO channels in indoor environments [20], [21].

TABLE I
Parameters of the RT solver.

Parameter	Reflections	Refractions	Diffractions	DoD spacing
Value	5	0	1	0.02°

1) Environment model: A simplified model of an indoor industrial environment consists of a cuboid volume (floorplan) with smaller cuboid scatterers distributed within it, similar to [22]. The floorplan has dimensions of 100 m×100 m×10 m. Dielectric properties of a concrete material at 3.5 GHz ($\varepsilon_r = 7$, $\sigma = 1.5 \cdot 10^{-2}$ S/m) were assigned to its floor, ceiling and walls [19]. The base of each scatterer has fixed dimensions of 2.5 m×1.25 m, and each scatterer height is selected independently from a uniform random distribution from 3 m to 7 m. The scatterers are positioned on a uniform

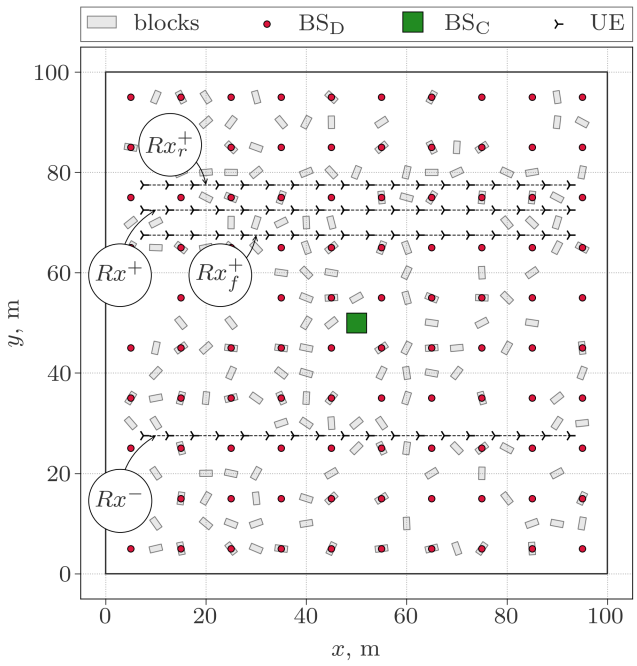

Fig. 1. The top view of the RT environment sample. The collocated (BS$_C$) and distributed (BS$_D$) Tx elements are drawn with the green square and red circles, respectively. The grey rectangles show the outlines of the cuboid scatterers. The UE tracks (Rx$^{+,-}$, Rx$_{f,r}^{+,-}$) are shown with black dashed lines, upon which the UE locations are marked with arrowheads, indicating the positive direction of the x-axis in the FDTD domain.

rectilinear grid with a step of 5 m in both x and y, and after that 30% of them is removed via random selection, which leaves around 88% of the floor surface unoccupied. Each of the remaining scatterers is then rotated at a random angle around the z-axis and assigned perfect electric conductor (PEC) material properties. The cuboid scatterers can be viewed as simplified models of a heavy industrial machinery or mobile robotic equipment (factories of the future setting), or metal storage racks (warehouse setting), that were placed without consideration for the potential APs locations.

All transmitter (Tx) antenna elements are assigned isotropic vertically-polarized (parallel to the z-axis) radiation patterns at $f_c = 3.5$ GHz central frequency ($\lambda \simeq 86$ mm). Two BS configurations are studied. The collocated BS (BS$_C$) is modeled with a 10-by-10 planar rectangular array of uniform half-wavelength ($\lambda/2$) inter-element spacing. The array surface is normal to the z-axis and its center was set at the center of the floorplan at $z = 9$ m, as indicated in Fig. 1. The distributed BS (BS$_D$) has identical parameters, except for the inter-element spacing, which was set to 10 m ($\simeq 116\lambda$) to uniformly cover the floorplan ceiling leaving a 5 m distance from any side-wall.

The receiver (Rx) positions form straight lines (tracks), crossing the floorplan parallel to the y-axis at the height of 1.65 m. A triplet of the Rx tracks (Rx$_f^+$, Rx$^+$, Rx$_r^+$ in Fig. 1), are located at $y = 67.5$ m, $y = 72.5$ m and $y = 77.5$ m, respectively, each consisting of 18 Rx points with x spanning from 7.5 m to 92.5 m with a uniform 5 m step.

In the next section the receivers from the *central* track of (Rx$^+$) triplet will function as the active targets of the

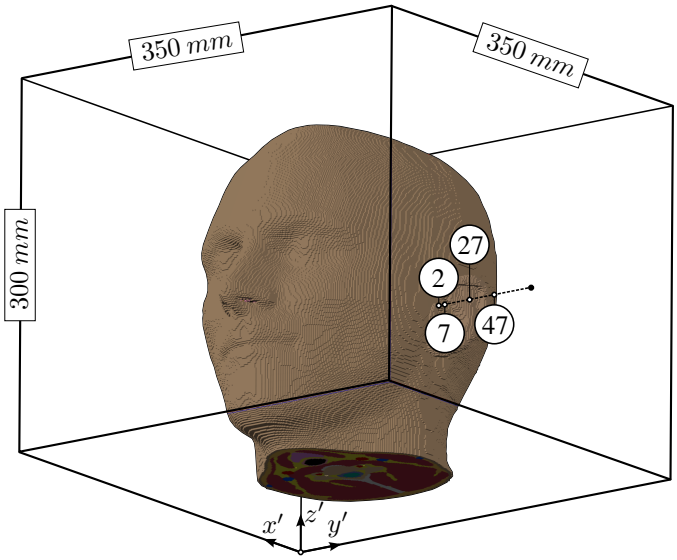

Fig. 2. The FDTD simulation domain. Voxels of the Duke phantom's head included in the domain are shown. The points at which the UE radiation pattern is evaluated are marked with white dots, and their distance to the head (in mm) is indicated.

BS transmission precoding, and their EMF exposure will be evaluated. The neighboring Rx positions at their *front* or *rear* side ($\mathrm{Rx}^{+}_{\mathrm{f,r}}$), relative to $\mathrm{BS_C}$, will act as interferers, to study exposure in scenarios where an interference-canceling scheme is used. Other interesting scenarios, in which the Rx track is aligned radially with respect to the collocated BS, were investigated in [22], [23].

A 0.02° ray-spacing is set to launch rays at each Tx point. Other RT simulation parameters are selected to assure the convergence of the RT results, while minimizing the total simulation run-time (summarized in Table I). These parameters follow the suggestions given in [24], except for the number of refractions, which are virtually non-existent with solely PEC scatterers.

Ten simulations were carried out, each with an independent random scatterer placement. The output of an RT simulation is a set of rays discovered for all Tx-Rx pairs $\{r_l^{rt}(\mathbf{E}_r, \theta, \varphi)\}_{kn}$, where $\mathbf{E}_r$ is the (complex) E-field strength or the ray with index l, θ and φ are its polar and azimuth DOA angles, and k, n are the indices tracking the Rx and Tx elements, respectively. These are used to calculate a narrow-band channel matrix $\mathbf{H}_{kn} \in \mathbb{C}^{K\times N}$, where K and N are the total Rx and Tx counts, respectively. The details of this procedure can be found in e.g. [25]. In addition, rays' DOA and the E-field strength are used to set the incident directions and relative amplitudes of the plane waves, that make up the exposure scenarios studied in the FDTD simulations, as described in the next section.

B. Finite-Difference Time-Domain

The FDTD method is employed to evaluate the DL radio-frequency (RF) EMF exposure of a user in proximity of its UE. The FDTD simulation domain is shown in Fig. 2. The domain bounding box is shown with solid black lines, having dimension of 350 mm by 350 mm by 300 mm. A heterogeneous human phantom model (ViP v.3.1 Duke [26]) is introduced into the domain as shown in Fig. 2. The head's bounding box is centered with respect to the domain in the xy-plane.

To interface the RT and the FDTD domains, a UE position is fixed relative to the phantom's head (some of the UE locations studied in the following sections are shown with white dots in Fig. 2). The head-UE separation distance is further denoted as δ. A UE location corresponds to the location of an Rx point in the RT simulation, and the directions of coordinate axes of both simulation domains coincide. For a fixed Rx point k, the RT solution provides a set of incident rays emanating from each Tx point n. DOAs of the incident rays are then resampled by replacing them with the outer normal vectors of an icosahedral sphere facets, to which they have the shortest angular distance. A more thorough description of the procedure outlined here can be found in [25]. An icosahedral sphere of frequency 2 [27] was used, which has $m = 220$ triangular facets. Thereafter, the resampled rays with matching DoAs are superimposed by taking a sum of their complex amplitudes, producing a reduced set of rays per Tx-Rx pair, which we further denote as $\{r_i\}_{kn}$. Performing this procedure for each Tx-Rx pair yields a resampled set of rays in an RT simulation $\{r_i\} = \bigcup\{r_i\}_{kn}$. Index i tracks the icosahedral sphere normal and therefore does not exceed the total number of the sphere's facets.

C. Channel matrix

This section explains how the channel matrix is calculated using rays at the Rx and the radiation pattern from the FDTD simulations.

The channel matrix $\mathbf{H}_{kn}$ is constructed using the resampled rays $\{r_i\}_{kn}$. Presence of the head disrupts the EMF at the UE obtained with the RT method (in free space). To take this into account, vertical component of the E-field E_z is sampled at the UE (at distance d from the head) from the single-plane-wave FDTD simulation performed for each of the resampled rays incidence directions, yielding a set of complex coefficients $A_i(d)$. According to the receive-transmit antenna reciprocity, A_i is proportional to the far-field radiation pattern of a small vertically-polarized dipole separated by distance d from the head in the DoA corresponding to the outer normal direction of the icosahedral sphere with index i.

Then, the channel coefficient h_{kn} between the Tx antenna with index n and the Rx antenna with index k is found as

$$h_{kn}(d) = \sum_{r\in\{r_i\}_{kn}} A_i(d)\tilde{E}_r^{\theta}, \tag{1}$$

and

$$\tilde{E}_r^{\theta} = E_r^{\theta}\exp(-2\pi j f_c \tau_r). \tag{2}$$

Here r tracks the index of all rays in $\{r_i\}_{kn}$, E_r^{θ} and τ_r are the elevation component (from the Rx point of view) of the E-field and the time-of-flight of the r^{th} ray, respectively.

Evaluating (1) for every Tx-Rx pair, we obtain the full massive MIMO channel matrix $\mathbf{H}(d)$ with a UE at distance d from the head.

D. Transmission precoding

A massive MIMO BS dynamically sets the amplitudes and phases of its antenna elements (according to the UE channels), which are described by the *transmit vector* $\mathbf{t} \in \mathbb{C}^{N\times 1}$. In general, $\mathbf{t}$ depends on the *precoding scheme* used by the BS, active UEs in the network with their channel coefficients, and symbols transmitted to (possibly a subset of) these UEs. In the following sections we analyze two precoding schemes: Maximum Ratio Transmission (MRT) and Zero-Forcing (ZF), *precoding matrices* [28] $\mathbf{W}$ of which are defined as

$$\mathbf{W} = \begin{cases} \mathbf{H}^H, & \text{for MRT,} \quad (3a) \\ \mathbf{H}^H(\mathbf{H}\mathbf{H}^H)^{-1}, & \text{for ZF,} \quad (3b) \end{cases}$$

where $(\cdot)^H$ denotes the conjugate transpose of a matrix. It is known that MRT results in the highest receiver signal-to-noise ratio (SNR) and is efficient in low interference noise-dominated channels [14]. On the other hand, ZF produces signals with the highest signal-to-interference ratio (SIR) and is advantageous when transmitting to UEs with highly correlated channel vectors [29].

The transmit symbols vector $\mathbf{s} \in \{0,1\}^{K\times 1}$ selects the UEs to which the transmission occurs (*target UEs*). Its length equals to the number of rows in the channel matrix, its k^{th} element equals 1 if the k^{th} UE is targeted, and 0 otherwise. With this we obtain the transmit vector as

$$\mathbf{t} = \alpha \mathbf{W}\mathbf{s}, \quad (4)$$

where α is a normalization coefficient that determines the total BS output power. In the following, α is always chosen such that $\mathbf{t}$ has unit norm, setting the BS output power to 1 W. Next section presents results of simulations relevant for each of the studied massive MIMO transmission schemes.

E. EMF distribution assessment

To determine the EMF distribution in proximity of the head and the UE, an FDTD simulation based on the RT output is performed. A ray with index r was modelled as a plane wave (PW) traversing the entire computational domain. For every direction i, an FDTD simulation with a single vertically-polarized PW is performed. We denote the resulting single-PW E-field distribution, normalized to the amplitude of the incident plane wave, as $\mathbf{e}_i(x,y,z)$.

To obtain the EMF distribution for the k^{th} UE in the DL of the BS, $\mathbf{e}_i(x,y,z)$ are superimposed with elements of the transmit vector t_n as weights.

$$\tilde{\mathbf{e}}_t(x,y,z) = \sum_{i=1}^{m} \left[\mathbf{e}_i(x,y,z) \sum_{n=1}^{N} t_n \left(\sum_{r\in\{r_i\}_{kn}} \tilde{E}_r^{\theta} \right) \right]. \quad (5)$$

Here, the inner-most sum is taken over the amplitudes of the (resampled) rays that share the incidence direction (index i in $\{r_i\}_{kn}$), and the outer-most sum combines the E-field distributions. Therefore, it is only necessary to sum at most m E-field distributions, which greatly reduces the computation time compared to using the full set of the RT rays directly. For a more detailed description of the FDTD simulation setup, its sensitivity and error analysis, see [22].

F. Exposure assessment

Evaluating (5) yields the E-field distribution in the FDTD domain. The ratio of the EMF power dissipated in the FDTD voxel to the mass of that voxel approximates the local Specific Absorption Rate (SAR). First, SAR is calculated in the phantom's tissues with the knowledge of their density and dielectric properties. Then, around each lossy voxel in the domain, the SAR is averaged over a cube containing 10 grams of media, according to the IEEE/IEC 62704-1 standard [30] (implemented internally in Sim4Life). Finally, the cube with the highest average SAR is determined (peak-cube). The corresponding SAR value is called peak-spatial SAR averaged over a 10-g cube ($\text{psSAR}_{10\text{g}}$). $\text{psSAR}_{10\text{g}}$ in the head is one of the quantities for which basic restrictions are specified by International Comission on Non-Ionizing Radiation (ICNIRP) [31]. The $\text{psSAR}_{10\text{g}}$ limit at 3.5 GHz for non-occupational exposure is 2 W/kg. In addition ICNIRP specifies the reference levels for the incident EMF power density (10 W/m^2). The power density below the reference level in the *far field* of an antenna is considered to result in the $\text{psSAR}_{10\text{g}}$ complying to the basic restrictions. Indeed, extensive numerical studies [32]–[34] in the sub-6 GHz frequency range, in which human phantoms were exposed to a *single* PW in full range of incident directions with vertical and horizontal polarization found $\text{psSAR}_{10\text{g}}$ in the head to closely approach the ICNIRP reference. It was also shown [25] that in favourable propagation conditions, a collocated 36-antenna BS array transmitting to a single UE with the MRT precoding, resulted in $\text{psSAR}_{10\text{g}}$ 5 dB lower on average than the ICNIRP basic restriction, with the BS power normalized such that the peak ('hot-spot') power density in the domain was 10 W/m^2. However, when normalized to the power density measured in free space, the $\text{psSAR}_{10\text{g}}$ was on average 10 dB higher than the ICNIRP basic restriction. In this contribution, we follow the approach proposed in [25] and introduce the normalized $\text{psSAR}_{10\text{g}}$, including the explicit dependence on the EMF sampling location, as

$$\eta[\frac{\text{m}^2}{\text{kg}}] = \frac{\text{psSAR}_{10\text{g}}[\text{W/kg}]}{\mathbf{s}(\mathbf{r})[\frac{\text{W}}{\text{m}^2}]}, \quad (6)$$

where $\mathbf{s}(\mathbf{r})$ is the time-averaged EMF power flux density at point $\mathbf{r}$. In proximity to a hot-spot the EMF may vary significantly over sub-wavelength distances. Therefore, the exact location at which the EMF is assessed (e.g., when measured for compliance testing) plays an important role, as shown further.

III. Results

This section presents the simulation results. First, the EMF distribution in vicinity of the head is discussed and its variation with the change of the UE-to-head distance is established. Then, we look at the EMF exposure and compare different normalization approaches. Lastly, we compare different transmission precoding strategies with the collocated BS_C and distributed BS_D layouts.

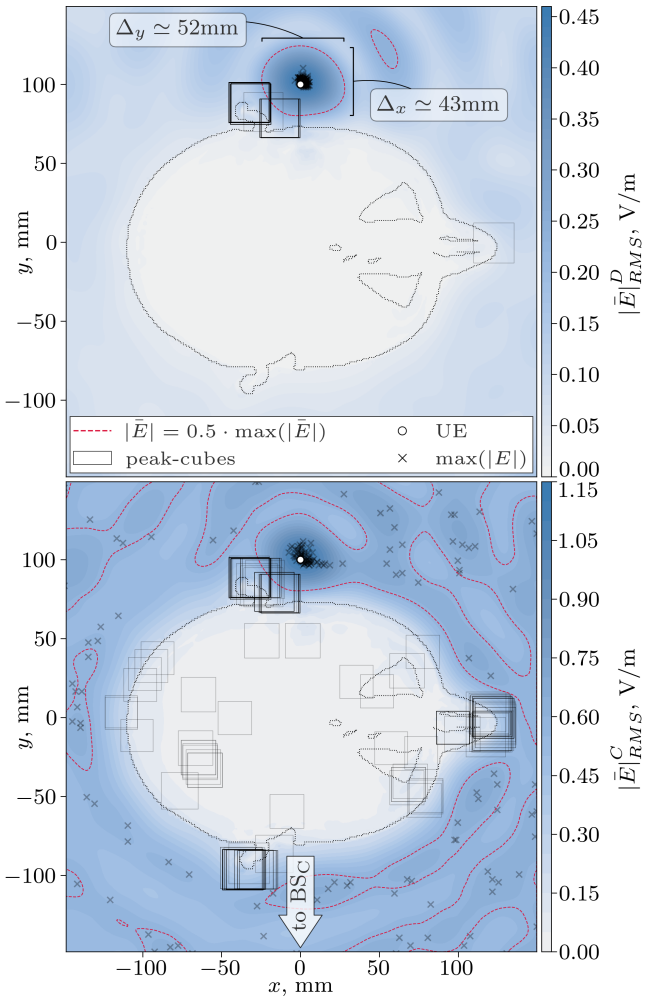

Fig. 3. Horizontal plane cross-section of the Rx$^+$ track-average RMS E-field with MRT precoding and $\delta = 27$ mm head-UE distance (top: BS$_D$, bottom: BS$_C$). The section plane z-coordinate coincides with the dipole center. At all UE positions from the Rx$^+$ track, the phantom head blocks the LOS paths to the collocated BS elements. The white circle marks the UE position. The black solid rectangles show the peak-cube sizes and positions. The black dotted line shows the outline of the phantom's head. The half-maximum sample-averaged E_{RMS} level is outlined with the dashed red lines. Additionally, the per-sample peak E_{RMS} locations are marked with black crosses. The direction towards BS$_C$ (center of the floorplan) is indicated with the arrow. The BS input power is 1 W at 3.5 GHz.

A. EMF Distributions

First, we examine the E-field focusing produced by the two studied BS layouts using the MRT precoding to target a single UE with a fixed 27 mm distance to the phantom's head δ (see Fig. 2). We consider the UE locations that belong to the Rx$^+$ and Rx$^-$ tracks (see Fig. 1). The arithmetic average of the root-mean-square (RMS) E-field (E_{RMS}) values taken over the UEs from one track approximates the time-average E-field of a user moving along that track with a constant speed in the direction indicated in Fig. 1 with arrows. Here, the effects of the non-zero UE speed on the channel are neglected, i.e. the movement is assumed to be quasi-static.

1) Hot-spot size: Fig. 3 shows the E_{RMS} in the horizontal slice coincident with the UE and averaged over the Rx$^+$ track in 10 environment samples (180 E_{RMS} samples per configuration). For all Rx locations in this track, the phantom's head blocks the LOS paths from all collocated BS antenna elements, thus shadowing the UE (Fig. 3, bottom). This is not the case for the distributed BS (Fig. 3, top), for which around a quarter of all Tx elements are in LOS, some of which are possibly blocked by the PEC scatterers in the environment. Nevertheless, due to a higher average propagation loss (larger average Tx-Rx distance) of the distributed BS, the maximum E-field produced by the collocated BS array exceeds it more than twofold, as indicated by the pseudo-color bars in Fig. 3.

The MRT precoding 'hot-spot' is centered around the UE location in both cases, marked with the white dot in Fig. 3. One parameter of interest we use to characterize the hot-spot is its half-maximum width in x and y directions, which we denote as Δ_x and Δ_y, respectively. Δ_x (Δ_y) is defined as the x (y) dimensions of the axes-aligned boundary box drawn around the contiguous region in which E_{RMS} exceeds its half-maximum level in the domain (the E_{RMS} threshold value). The red dashed contours in Fig. 3 show the E_{RMS} half-maximum level. The time-average hot-spot is clearly identified for the distributed BS topology, and $\Delta_x \simeq 52$ mm ($\simeq 0.6\lambda$), $\Delta_y \simeq 43$ mm ($\simeq 0.5\lambda$), as indicated (Fig. 3, top). With the collocated BS, the half-maximum boundaries extend outside the FDTD domain. This is caused by a relatively high (approaching the half-maximum value) *background* E_{RMS}, i.e. the E-field levels observed in proximity of the head, but outside of the peak E_{RMS} neighborhood.

We then examine the distribution of the *instantaneous* Δ_x and Δ_y over those samples for which the averaging was performed. The Cumulative Distribution Functions (CDFs) of Δ_x and Δ_y for the two BS layouts and two Rx tracks are shown in Fig. 4.

We first discuss the hot-spot size distributions for the UEs on the Rx$^+$ track. In the distributed BS configuration transmitting to Rx$^+$, nearly no instantaneous hot-spots are larger than 100 mm ($\simeq 1.1\lambda$) in x and 75 mm ($\simeq 0.9\lambda$) in y (black and red solid lines in Fig. 4). Their distributions' median value approximately equals the hot-spot size calculated for the sample-average E_{RMS}, indicating that the hot-spot shape and position are consistent throughout the E_{RMS} samples. The median value of Δ_x^C and Δ_y^C (green and blue solid lines in Fig. 4) is slightly above 70 mm, and 51 mm, respectively, which is larger than what is found with the distributed BS. Importantly, a significant portion of hot-spots extends outside the FDTD domain. For Δ_x^C that means having values greater than 150 mm (nearly 20% of samples) and for Δ_y^C - greater than around 75 mm (approximately 30% of samples). This shows that in some cases the collocated BS produces notably worse E-field focusing, which might result from its propagation diversity deficiency, i.e. narrow DoA spread shared by a large fraction of the collocated BS elements.

The superior focusing produced by BS$_D$ in comparison with BS$_C$ is also reflected in the distribution of the psSAR$_{10g}$ peak-cube locations (shown with black squares in Fig. 3). In all BS$_D$ exposure samples, the peak-cube is found around the left ear, in the immediate proximity to the E_{RMS} maximum, all of which are clustered around the UE (Fig. 3, top). The peak-cubes found with BS$_C$ are found in approximately equal

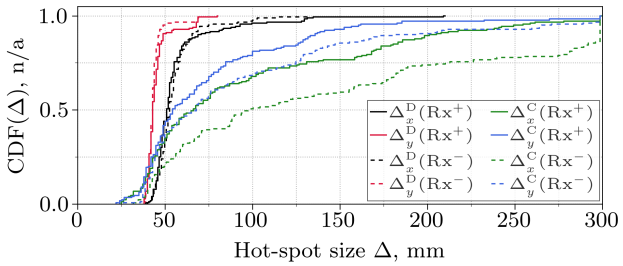

Fig. 4. Cumulative distributions of the hot-spot widths Δ at half-maximum in x and y directions for Rx^+ (solid) and Rx^- (dashed). Hot-spots produced by the distributed BS are displayed in black (Δ_x^D) and red (Δ_y^D). The collocated BS Δ are shown in green (Δ_x^D) and blue (Δ_y^D).

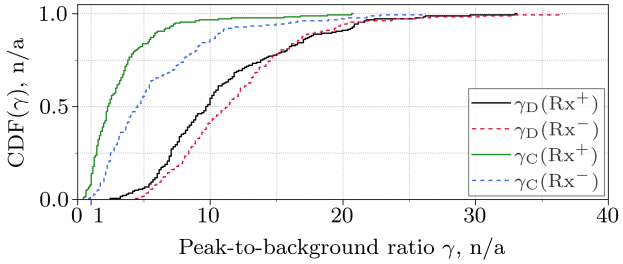

Fig. 5. Cumulative distributions of the peak-to-background ratios γ for Rx^+ (solid) and Rx^- (dashed). The values obtained with $\mathrm{BS_D}$ are displayed in solid black ($\gamma_D(\mathrm{Rx}^+)$) and dashed red ($\gamma_D(\mathrm{Rx}^-)$). The values obtained with $\mathrm{BS_C}$ are displayed in solid green ($\gamma_C(\mathrm{Rx}^+)$) and dashed blue ($\gamma_C(\mathrm{Rx}^-)$).

portions around both ears and the nose, the organs in which $\mathrm{psSAR_{10g}}$ is found under plane-wave exposure [32]. This indicates that in scenarios with $\mathrm{BS_C}$ the locations of the actual averaged absorption maxima are not correlated with the E-field maxima locations.

We also look at the hot-spot properties of the Rx^- track. The distributions of $\Delta_x^D(\mathrm{Rx}^-)$ and $\Delta_y^D(\mathrm{Rx}^-)$ (black and red dashed lines in Fig. 4) are almost identical to those of $\Delta_x^D(\mathrm{Rx}^+)$ and $\Delta_y^D(\mathrm{Rx}^+)$, respectively, with slightly fewer $\Delta_y^D(\mathrm{Rx}^-)$ samples having values above 50 mm. Interestingly, the collocated BS performs worse for the Rx^- track compared to the Rx^+ track. This is especially distinct in case of $\Delta_x^C(\mathrm{Rx}^-)$ (green dashed line), for which the median value is around 100 mm, and around a quarter of all samples approaches 300 mm. The distribution of $\Delta_y^C(\mathrm{Rx}^-)$ is nearly identical to that of $\Delta_x^C(\mathrm{Rx}^+)$. As more antenna elements of the collocated BS reach Rx^- in LOS, experiencing less reflections, the DoA diversity is further reduced, resulting in worse EMF focusing. However, it is clear that Δ is sensitive to the choice of the E_{RMS} threshold value for the hot-spot size evaluation.

2) Peak-to-background ratio: Another metric with which we characterize the EMF focusing is the E_{RMS} peak-to-background ratio γ. We calculate it by taking the ratio of the maximum E_{RMS} in the domain (hot-spot) to the E_{RMS} value at the location symmetrical to the maximum location with respect to the phantom's head mid-saggital plane, which is also (approximately) a symmetry plane of the phantom's head. Therefore, γ quantifies a small-scale E_{RMS} gain that the massive MIMO precoding achieves by comparing E_{RMS} at two locations equivalent with respect to the geometry in their closest vicinity. Fig. 5 shows CDFs of γ for different BS layouts transmitting to different Rx tracks. All samples of γ in every configuration have values greater than one, meaning that the MRT precoding always enhances the signal strength at the UE side of the phantom's head, compared to the opposite side. This is indeed not a trivial result, in particular in scenarios with the collocated BS. For example, the Rx in the center of Rx^+ has around 60% of all power incident from the right side (direction to the BS). This would result in $\gamma < 1$ due to the effect of shadowing by the phantom's head, if not for the BS transmission precoding. As a reference, if exposed by a single plane wave propagating in the positive direction of the y-axis, γ can be as low as 0.25. However, the median value of $\gamma_C(\mathrm{Rx}^+)$ is only slightly above 2, which explains why the hot-spot cannot be clearly resolved at its half-maximum level: at least half of the time E_{RMS} enhancement is not strong enough. The median of $\gamma_C(\mathrm{Rx}^-)$ is just below 5, the shadowing effect in this case aids the E_{RMS} focusing.

With the BS in the distributed configuration, significantly higher values of γ are observed. The median values of $\gamma_D(\mathrm{Rx}^+)$ and $\gamma_D(\mathrm{Rx}^-)$ are around 10 and 12, respectively. The difference between the tracks is not as pronounced as with the collocated BS. Indeed, with the BS antennas distributed at the ceiling, though the UE at the Rx^+ track is facing around three times more antenna elements than the UE at the Rx^- track, most of these extra antenna elements are also considerably further away from the UE, which reduces their contribution to the total incident power.

B. Head-to-UE distance

To generalize the results obtained in the previous section, we repeat the same set of simulations that was executed for $\delta = 27$ mm for four more UE-head separation distances $\delta \in \{2\text{ mm}, 7\text{ mm}, 12\text{ mm}, 47\text{ mm}\}$. The E_{RMS} distributions in proximity of the hot-spot are compared for $\delta \in \{7\text{ mm}, 27\text{ mm}, 47\text{ mm}\}$ with $\mathrm{BS_D}$ (top row) and $\mathrm{BS_C}$ (bottom row) of Fig. 6. The FDTD domain is cropped such that only its portion around the UE (white dot in Fig. 6) is shown in each configuration. In addition, the red cross marks the location of the peak E_{RMS} in the hot-spot, which we consider to be the hot-spot center.

It is clear that the hot-spot (on average) is not centered around the UE for $\delta \in \{7\text{ mm}, 47\text{ mm}\}$. The hot-spot position and shape for $\delta = 7$ mm are nearly identical to those when $\delta = 27$ mm, as can be seen comparing the left and the center columns of Fig. 6. With the UE further away from the head ($\delta = 47$ mm), the hot-spot increases in size in the y-direction, and at the same time its center is shifted towards the UE (but does not coincide with it). These results are counterintuitive: one would expect the MRT precoding to ensure the optimal constructive interference of the incident EMF at the UE location, and the large BS antenna count - to make the same unlikely at any other location.

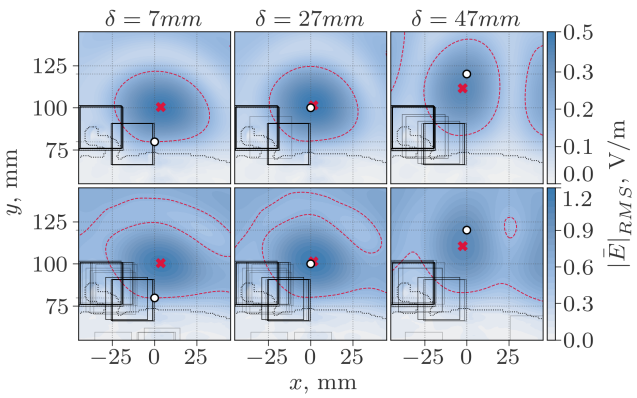

Fig. 6. The average E_{RMS} hot-spots for different head-UE separation distances δ. The top and bottom rows show scenarios with BS_D and BS_C array layout, respectively. The value of δ is fixed in each column and indicated at the top. Other markers have the same meaning as defined in Fig. 3. In addition, the peak sample-averaged E-field location is marked with the red cross.

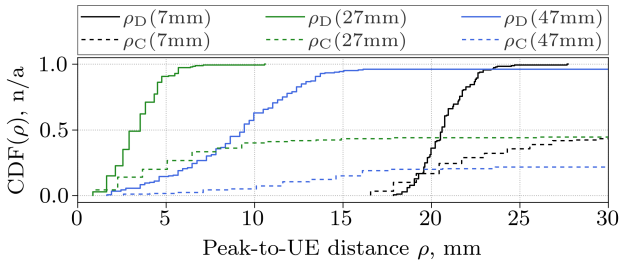

Fig. 7. Cumulative distributions of the hot-spot center distance from the UE ρ for Rx^+. Hot-spots produced by the BS_D and BS_C are drawn with solid and dashed lines, respectively. The black, blue, and green lines show ρ for scenarios with $\delta = 7$ mm, 27 mm, and 47 mm, respectively.

1) Peak-to-UE distance: To study this effect in more detail, in Fig. 7 we plot the CDFs of the distance ρ from the instantaneous hot-spot to the UE calculated for the 6 configurations shown in Fig. 6.

Interestingly, with the BS_C configuration irrespective of the UE-to-head distance δ, in around half of all samples the hot-spot peak was not found near the UE (ρ_C in Fig. 7). However, this does not mean that the collocated BS often fails to produce the EMF gain at the UE (as Fig. 5 shows the opposite). This rather suggests that the gain is not strong enough to overturn the EMF peaks that occur naturally (e.g., in single-PW exposure scenarios [32]) near the irregular the anatomical features of the phantom model (i.e., ears' edges, nostrils).

The distributed BS forms a hot-spot around the UE at $\rho = 27$ mm with the accuracy of around 5 mm in almost all simulated samples (green solid line in Fig. 7). If the UE is 47 mm away from the head, nearly in all cases the hots-pot peak was not further than 15 mm from it (not exceeding 10 mm most of the time). However, with the UE very close to the head ($\delta = 7$ mm, black solid line in Fig. 7), the hot-spot was never found around it. The similarity of the average EMF distributions in Fig. 6 and, at the same time, the shapes of the CDFs of ρ for scenarios with $\delta = 7$ mm and $\delta = 27$ mm

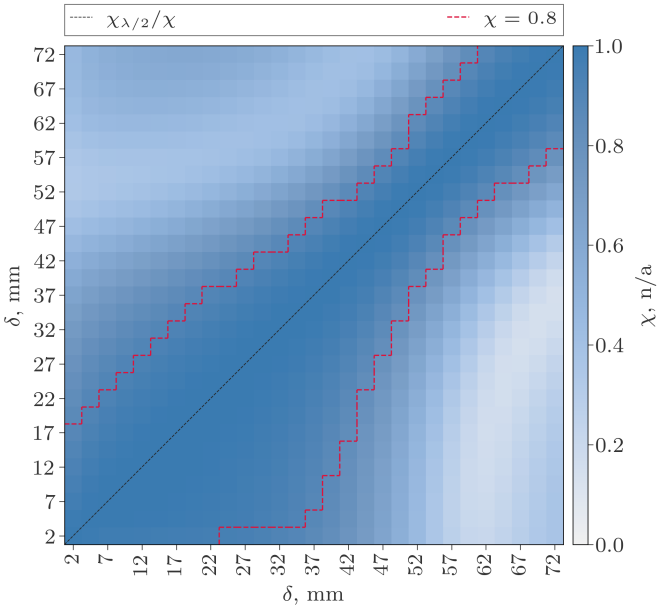

Fig. 8. Correlation matrix of the UE radiation pattern as a function of the UE-head separation distance δ. The top-left and the bottom-right triangles (delimited by the dashed black line) show the matrices corresponding to the half-wave ($|\mathbf{A}|_{\lambda/2}(d)$) and the small dipole ($|\mathbf{A}|(d)$) antennas, respectively. The red dashed lines mark the boundary of the region where the correlation crosses the 80% level.

suggests that, in fact, a nearly identical transmission precoding is performed by BS_D.

2) Radiation pattern correlation: To understand how this happens we examine the evolution of the UE radiation pattern ($A_i(d)$ in (1)) as it moves further away from the head (along the black dashed line in Fig. 2). We calculate the correlation coefficient

$$\chi(d_j, d_k) = \frac{\sum_i^m |A_i(d_j) A_i^*(d_k)|}{\sum_i^m |A_i(d_j)||A_i(d_k)|}, \tag{7}$$

where $(\cdot)^*$ denotes the complex conjugate, and $|\cdot|$ is the absolute value of a complex number. In (7), the icosahedral sphere facet normal index i tracks the components of the radiation patterns, viewed as vectors $\mathbf{A} = [A_1, A_2, \ldots, A_m]^T \in \mathbb{C}^{m\times 1}$. The closer $\chi(d_j, d_k)$ is to unity, the more similar $\mathbf{A}(d_j)$ and $\mathbf{A}(d_k)$ are. Equation (7) is first evaluated with the electrically small antenna pattern for $d = \delta \in [2\text{ mm}, 72\text{ mm}]$. In addition, we also evaluate (7) with the radiation pattern $\mathbf{A}_{\lambda/2}(d)$ of the half-wave dipole model, centered at the small dipole location (calculated with a dedicated FDTD simulation). Fig. 8 shows $\chi(d_j, d_k)$ matrices of the short (below the diagonal) and the half-wave (above the diagonal) dipoles. The correlation is strong ($\chi(d_j, d_k) \simeq 1$ for $d_j \simeq d_k$) for both dipole models, and the near-diagonal elements are close to 1. The red dashed line in Fig. 8 delimits the area, within which χ exceeds 80%.

Interestingly, the short dipole radiation pattern is highly-correlated for all values of δ from 2 mm to around 35 mm. Therefore, the channel matrix (1), the precoding matrix (3a), and hence the BS transmit vector (4), do not change significantly with the small dipole position in that range. This explains the similarity of the EMF distributions in the hot-

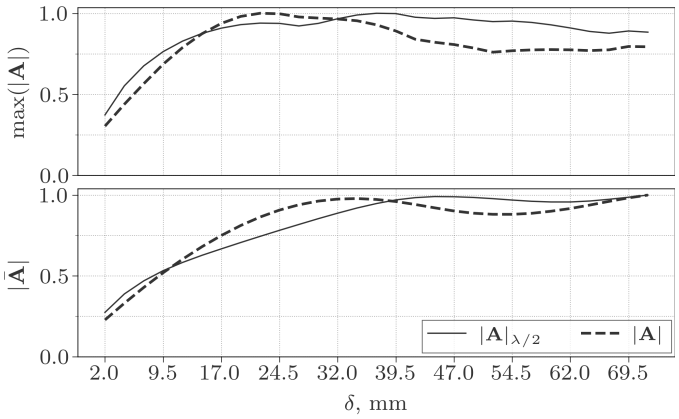

Fig. 9. UE directivity magnitude as a function of the UE-head separation distance. Solid and dashed lines show the half-wave ($|\mathbf{A}|_{\lambda/2}(d)$) and the small dipole ($|\mathbf{A}|(d)$) values, respectively. Top: maximum pattern magnitude (directivity). Bottom: pattern magnitude averaged over the direction of arrival.

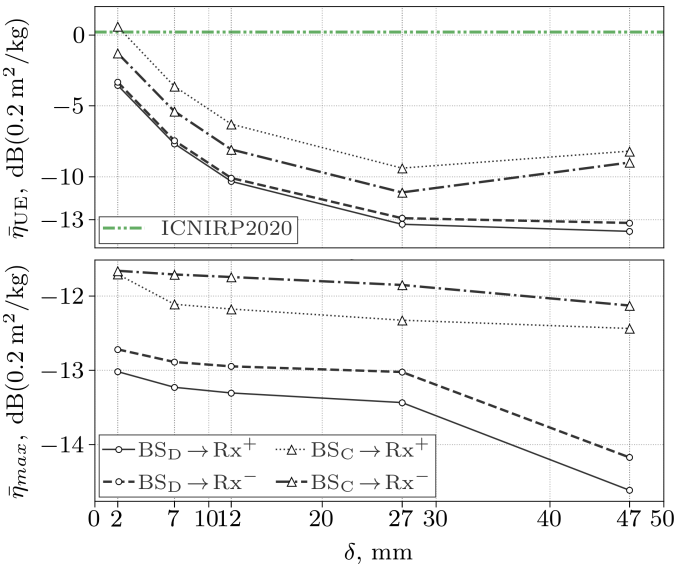

Fig. 10. The sample-average psSAR$_{10g}$ normalized to the time-average power density (η) at the UE location (top) or at the FDTD domain maximum (bottom), as a function of δ. η in scenarios with BS$_{\mathrm{D}}$ (BS$_{\mathrm{C}}$), calculated for the Rx^{+} and Rx^{-} tracks are shown with the black solid (dotted) and dashed (dash-dotted) lines with circle (triangle) markers, respectively. In addition, η calculated from the ICNIRP basic restrictions and reference levels is shown with the dash-double-dotted horizontal green line, indicating the dB reference value.

spots for $\delta = 7$ mm and $\delta = 27$ mm in Fig. 6: the BS transmits with almost the same weight.

To explain why the hot-spot is observed consistently around the small dipole at $\delta = 27$ mm and *not* at $\delta = 7$ mm, even when the latter was targeted, we also plot the arithmetic mean ($|\bar{\mathbf{A}}| = \frac{\beta_1}{m}\sum_i^m |A_i(d)|$) and the maximum magnitudes $\max(|\mathbf{A}|) = \max_i |A_i(d)|$, as (normalized with β_1 and β_2) functions of δ, shown in Fig. 9.

Both the average and the maximum magnitude of the small dipole pattern decrease rapidly as it approaches the head (dashed black lines in Fig. 9). $A_i(\delta)$ are defined as the E_{RMS} measured at distance δ from the phantom's head after it is exposed with a plane wave incident with the DoA i (see section II-C). Taken together with the observation in the previous paragraph, this means that the combination of plane waves interfering constructively close to the head (e.g., at $\delta = 7$ mm), combine (nearly as) constructively, but with a larger amplitude further away (e.g., at $\delta = 27$ mm). Quantitatively, as shown in Fig. 9, at $\delta = 7$ mm both $|\bar{\mathbf{A}}|$ and $\max(|\mathbf{A}|)$ are approximately two times smaller than at $\delta = 27$ mm, where they (nearly) reach their maximum. This agrees well with what is shown in the first two columns of Fig. 6.

At even larger distances from the head (e.g., $\delta = 47$ mm shown in the third column of Fig. 6), the correlation of $\mathbf{A}$ decreases considerably (down to around 67% relative to $\delta = 27$ mm), while $|\bar{\mathbf{A}}|$ and $\max(|\mathbf{A}|)$ are only around 10% lower, as can be seen from Figs. 8 and 9. Hence, it is possible to produce the hot-spot more accurately at $\delta = 47$ mm, although its peak is infrequently observed as far as 15 mm away from the true UE location, as shown in Fig. 7 (solid blue line).

The half-wave dipole's radiation pattern $\mathbf{A}_{\lambda/2}(d)$ correlation and magnitudes are shown in Figs. 8 (upper triangle) and 9 (solid black lines), respectively. $\mathbf{A}_{\lambda/2}(d)$ exhibits more variation (Fig. 8), especially at small δ, compared to $\mathbf{A}(d)$, possibly due to its larger size. This could help to decorrelate two closely spaced receivers near the head, e.g., in a multi-antenna UE. The variation of $|\mathbf{A}|_{\lambda/2}(d)$ (Fig. 9) is qualitatively similar to that of $|\mathbf{A}|(d)$, though in this case it cannot be directly related to E_{RMS} at a single point (the UE location).

In the next section we analyze the exposure in the hot-spots produced with the small dipole.

3) Peak-spatial SAR: This section presents η the peak-spatial SAR averaged over a 10 g cube (psSAR$_{10g}$), normalized to the time-averaged power flux density ($\mathbf{s}(\mathbf{r})$), as defined in (6). As mentioned in Section II-F, it is important to keep track of the point $\mathbf{r}$ at which $\mathbf{s}$ is sampled, as the time-averaged EMF levels may vary significantly in vicinity of a hot-spot. In this section two normalization strategies are compared. First, $\mathbf{s}_{\mathrm{UE}} = \mathbf{s}(\mathbf{r}_{\mathrm{UE}})$ is measured at the UE location, which is known in advance in each scenario. Second, the maximum of $\mathbf{s}(\mathbf{r})$ over the complete FDTD domain ($\mathbf{s}_{max}$) is taken. The location of the maximum $\mathbf{r}_{max}$ is determined for each sample, and often is not found close the UE, especially with BS$_{\mathrm{C}}$, as mentioned in Section III-B1 and is seen in Fig. 7. Fig. 10 shows the sample-average values of η_{UE} (top) and η_{max} (bottom), for the BS$_{\mathrm{D}}$ and BS$_{\mathrm{C}}$ configurations, averaged over the Rx^{+} and Rx^{-} UE tracks.

The psSAR$_{10g}$ normalized with both strategies is higher in scenarios with BS$_{\mathrm{C}}$ than in the corresponding scenarios with BS$_{\mathrm{D}}$. The sample-average of η_{max} with BS$_{\mathrm{C}}$ (Fig. 10, bottom) slightly decreases with δ, staying around 12 dB lower than the ICNIRP reference (0.2 m^2/kg) for both Rx^{+} (dotted line) and Rx^{-} (dash-dotted line). For BS$_{\mathrm{D}}$, the sample-average of η_{max} is approximately constant and around 13 dB below the ICNIRP reference for $\delta \in [2\mathrm{mm}, 27\mathrm{mm}]$ and drops to around 14 dB below the ICNIRP reference at $\delta = 47$ mm.

In contrast to that, the sample-average of η_{UE} goes up rapidly at small δ. However, this is only due to the fact that it

is less likely to find the peak EMF near the UE for $\delta < 27$ mm, as was discussed in Section III-B1. Thus, while the average $\text{psSAR}_{10\text{g}}$ does not increase at small δ, the EMF at the UE location decreases, causing the increase of the normalized quantity η_{UE}. $\hat{\eta}_{\text{UE}}$ with BS_C and Rx^+ (the collocated BS and the UE blocked by the head) reaches the ICNIRP reference at $\delta = 2$ mm (dashed line in Fig. 10, top), and falls to the level of around -10 dB at $\delta \geqslant 27$ mm. $\hat{\eta}_{\text{UE}}$ is around 2 dB lower than the values of Rx^+ at all δ for BS_C transmitting to Rx^- (dash-dotted line). With BS_D, $\hat{\eta}_{\text{UE}}$ has nearly equal values in scenarios with Rx^+ and Rx^- (solid and dashed lines in Fig. 10, top), reaching their maximum of around -4 dB at $\delta = 2$ mm and falling to around -13 dB at $\delta = 27$ mm (where it coincides with $\hat{\eta}_{max}$).

$\hat{\eta}_{\text{UE}}$ can be interpreted as the normalized $\text{psSAR}_{10\text{g}}$ under the assumption that the BS performing the power control that maintains the received signal level at the UE. As the UE close to the user head cannot be accurately focused towards, the BS is bound to raise the output power, which increases $\text{psSAR}_{10\text{g}}$. In addition, site-specific RT simulations with realistic BS/UE parameters could be used to estimate the DL exposure by measuring the UE received power only. By simulating the EMF distribution around the phantom head and then using the UE measurements (at a known position with respect to the head) as the calibration factor, the $\text{psSAR}_{10\text{g}}$ can be determined. It is worth pointing out that currently the reference levels are assessed in free space, according to the ICNIRP guidelines. The presented results indicate that it is essential to carefully consider both the UE and the user body position relative to each other and the BS, to accurately measure the actual peak EMF levels.

C. Zero-Forcing

In this section the ZF transmission scheme is studied in multi-user scenarios. Three scenarios were defined.

In the first scenario, the BS simultaneously transmits to three UEs, the locations of which are selected from a separate Rx track of the Rx^+ triplet (Rx^+, Rx_f^+ and Rx_r^+, as shown in Fig. 1), such that their x-coordinates are equal. This way, each of the three UEs is likely to observe similar DoA distributions in scenarios with BS_C. This is expected to increase their inter-channel correlation, thus reducing the BS's multiplexing efficiency. We evaluate the exposure of the UE in the central Rx^+ track, referring to this scenario as *Target*, as the BS in this scenario targets the studied UE. To calculate the transmit weights, first the reduced channel matrix is constructed by evaluating (1) for the three selected receiver indices k. Then, the precoding matrix is calculated as (3b). The symbol vector elements are in this case all equal to 1, as each UE in the channel is targeted. Lastly, the transmit vector is calculated with (4), and the EMF distribution is evaluated as described in Section III-A. This scenario evaluates the EMF incident at the UE due to the transmission directed to it and the two more neighboring UEs.

In the second scenario, we evaluate the EMF incident at the UE from the Rx^+ track (where a zero is formed) due to the transmission only to the other two UEs (from tracks Rx_f^+ and Rx_r^+). To achieve that, the symbol vector elements corresponding to the indices of the UEs from Rx_f^+ and Rx_r^+ are set to 1, and the single element corresponding to the Rx^+ track is set to 0. The remainder of the procedure is identical to the one of the Target scenario. This scenario is further referred to as *Interferer*. It is worth pointing out that this scenario is unlikely to occur in practice, as it is not beneficial to minimize the interference to a UE if it is not receiving at the moment (and thus no need to include that UE in the channel matrix). However, it allows to compare the exposure induced only by the interference-cancelling part of the transmission in distributed and collocated systems.

The third scenario, to which we further refer as *Non-user*, differs from the Target scenario in that it only includes the UEs from Rx_f^+ and Rx_r^+ tracks in the channel matrix. As before, the EMF is evaluated at a location in Rx^+, though in this case no UE is present there. This scenario is practically relevant, evaluating the exposure of a non-user surrounded by active users.

Fig. 11 shows the sample-average EMF distributions for the Target, Interferer and Non-user scenarios in the first, second and third columns, respectively.

1) Distributed BS: The distributed BS (top row of Fig. 11) forms a hot-spot near the target UE (Fig. 11, top-left) with the half-maximum size and shape nearly identical to the one found with the MRT precoding (Fig. 3, top). In only three out of 180 samples, the instantaneous E_{RMS} maximum (the black crosses in Fig. 11) was found outside the hot-spot half-maximum sample-average region (the dashed red lines in Fig. 11). This indicates that the BS_D is able to efficiently multiplex three closely-spaced UEs, i.e., the simultaneous transmission to two extra UEs does not alter the EMF distribution around the UE under consideration.

The same conclusion is drawn looking at the CDF of the peak-to-background ratio in the Target configuration with BS_D γ_D^T (red solid line in Fig. 12). In all samples, γ_D^T is found to be greater than 1, meaning that, as was found with the MRT scheme (Fig. 5, solid red line), the ZF precoding consistently boosts E_{RMS} around the UE, compared to the corresponding location at the other side of the user head. The median value of γ_D^T is around 8 dB, which is about 2 dB lower than that of $\gamma_D(\text{Rx}^+)$. This likely results from the interference cancellation achieved by the ZF scheme, which reduces the interference portion of the total E_{RMS} only at the UEs' locations, and not anywhere else (e.g., the opposite side of the user head). This decreases their ratio γ_D^T.

The distribution of the interference portion of the total $\bar{E}_{\text{RMS}}$ (the Interferer UE scenario) is shown in the top-center of Fig. 11. An area of a reduced $\bar{E}_{\text{RMS}}$ levels (relative to the $\bar{E}_{\text{RMS}}$ levels in the surrounding space) is formed close to the left side of the phantom's head, encompassing the location of the UE, as shown with the red dashed half-maximum $\bar{E}_{\text{RMS}}$ contour in Fig. 11. The CDF of γ_D^I (solid green line in Fig. 11) shows that in around half of all samples, the E_{RMS} around the UE is at least 4 dB (2.5 times) lower than that observed at the opposite side of the head. The instantaneous E_{RMS} peak and the $\text{psSAR}_{10\text{g}}$ peak-cube locations are distributed widely around the head and largely determined by the head's irregular

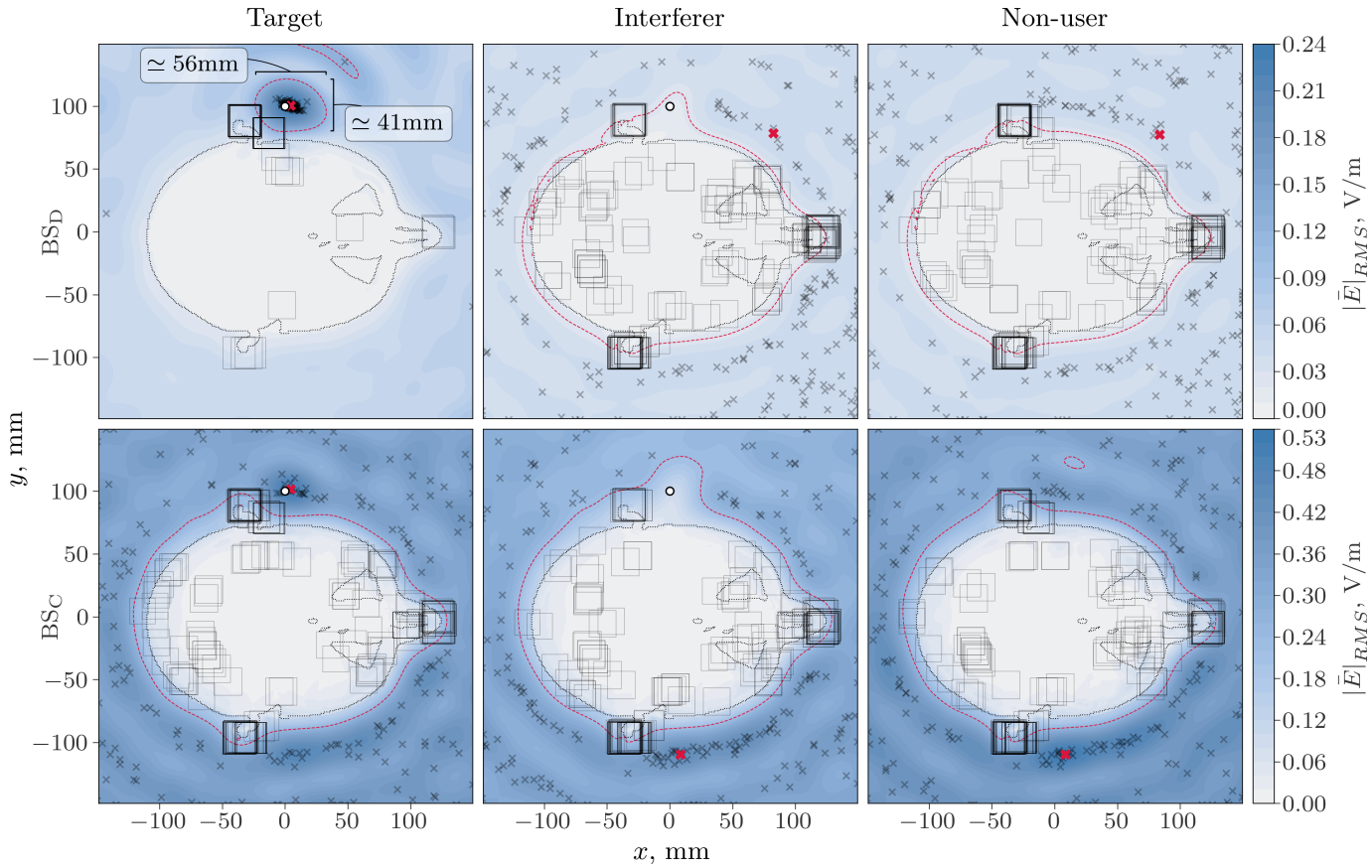

Fig. 11. Horizontal plane cross-section of the Rx$^+$ track-average RMS E-field with multi-user ZF precoding at $\delta = 27$ mm (top row: distributed BS, bottom row: collocated BS). The first, second, and third column show the Target, Interferer, and Non-user scenarios, respectively. Other markers have the same meaning as defined in Fig. 3.

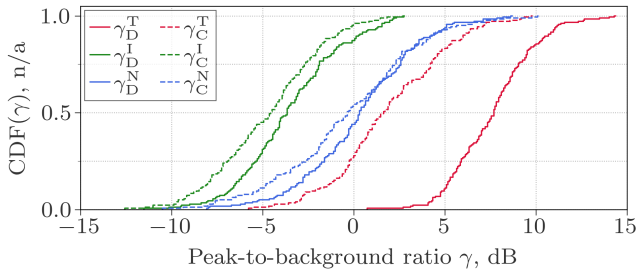

Fig. 12. The CDFs of the peak-to-background ratio γ for the UEs from the Rx$^+$ track in Target (T, red), Interferer (I, green) and Non-user (N, blue) configurations. The $\mathrm{BS_D}$ and $\mathrm{BS_C}$ configuration CDFs are shown with solid and dashed lines, respectively.

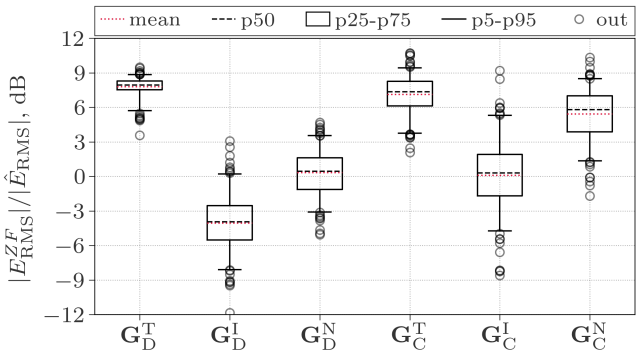

Fig. 13. Distribution parameters of the ZF gain relative to the non-coherent BS transmission with the same total power of 1 W. The dashed lines, boxes and whiskers show the 50$^{\text{th}}$, 25$^{\text{th}}$-75$^{\text{th}}$, 5$^{\text{th}}$-95$^{\text{th}}$percentiles, and the remaining samples (outliers) are plotted with circles. The distributed (D) and collocated (C) BS configurations in the Target (T), Interferer (I) and Non-user (N) scenarios are labeled below the horizontal axis.

features and the power distribution of the incident rays' DoAs.

In the Non-user scenario (Fig. 11, top-right) the $\bar{E}_{\mathrm{RMS}}$, peak E_{RMS}, and $\mathrm{psSAR_{10g}}$ peak-cube distributions are approximately symmetrical with respect to the x-axis. It can be also seen in Fig. 12, that the CDF of γ_D^N (solid blue line) has the median (and mean) value close to 0 dB. This means that the E_{RMS} levels are, on average, equal on two sides of the phantom's head with the distributed BS transmitting to two UEs, each 5 m away from the studied location (the Non-user scenario). Indeed, it appears that in this case $\bar{E}_{\mathrm{RMS}}$ is not affected by the transmission to the UEs nearby.

To validate this assumption, we calculate the *spatial diversity* E-field gain $\mathbf{G}$ at the UE location $(0, \delta, 0)$ as a ratio between the E_{RMS} observed at that location and a non-coherent sum of the RMS E-field induced by the BS's individual antenna elements $\hat{E}_{\mathrm{RMS}}$, obtained as

$$\hat{E}_{\mathrm{RMS}} = \frac{1}{\sqrt{N}} \sum_{n=1}^{N} \left(\sum_{i=1}^{m} \mathbf{e}_i(0,\delta,0) \sum_{r \in \{r_i\}_{kn}} \tilde{E}_r^{\theta} \right)_{\mathrm{RMS}} . \quad (8)$$

This expression differs from (5) in the following:

- The sum over the Tx index is taken last.
- The individual Tx element's contributions are summed in their RMS values.
- The transmit vector elements are all equal to $1/\sqrt{N}$.
- The ico-ray E-field distributions are sampled at the UE location $(0, \delta, 0)$ prior to summation.

Taking the two inner-most sums of the complex-valued E-field contributions of the rays originating from the same Tx element (index n) accounts for the fast-fading propagation effects, i.e., the multipath inter-ray interference. Time-averaging the E-field before taking the outer-most sum eliminates the Tx inter-antenna interference, that gives rise to the MIMO multiplexing gain. The equal transmit weights preserve the overall 1 W BS power normalization. $\hat{E}_{\mathrm{RMS}}$ can be viewed as the average over a large number E-field observations in which the BS elements transmit with equal power and independent random phases. If the BS size is much smaller than the distance to the point at which the E-field is assessed (e.g., the $\mathrm{BS_C}$ configuration), $\hat{E}_{\mathrm{RMS}}$ also approximates the time-averaged E-field induced by a single-antenna BS at the center of the original antenna array, transmitting with equal total power.

The statistical properties of the multiplexing gain sample distributions are shown as the bar-plots in Fig. 13 for all the studied ZF scenarios. The mean and median value of $\mathbf{G}_D^N$ is indeed very close to 0 dB, meaning that the ZF transmission of $\mathrm{BS_D}$ does not affect the average E-field levels at non-user locations (at least 5 m away a target UE). The mean and median diversity gain at the target UE achieved by $\mathrm{BS_D}$ is around 8 dB, which is close to the peak-to-background ratio in this scenario. This allows to conclude that the E-field at the side of the head opposite to the UE does not differ, on average, from the E-field at a non-user location, i.e., in the distributed BS configuration the E-field is decorrelated at short separation distances (smaller than the phantom's head size). The average Interferer gain is -4 dB, which is also close to γ_D^I, and exceeds 0 dB only 5% of the time.

An important characteristic of the ZF precoding scheme in multi-UE scenarios is the SIR (it is known that ZF minimizes it). The average SIR can be estimated from Fig. 13 as the difference between the mean gain in the Target and Interferer scenarios. Therefore, the average SIR is estimated at around 12 dB for $\mathrm{BS_D}$.

2) Collocated BS: The collocated BS configuration yields the average Target UE gain just below 8 dB ($\mathbf{G}_C^T$ in Fig. 13), close to what is found for $\mathrm{BS_D}$. However, as can be seen in Fig. 11 (bottom-left), the instantaneous E_{RMS} maxima often occur in locations away from the UE. Comparing this to Fig. 3 (bottom), in which a significant portion of the E_{RMS} maxima is adjoint to the UE, we conclude that in the studied multi-user ZF scenario with $\mathrm{BS_C}$, the hot-spot is largely disrupted by the interference with the nearby UEs. This is also confirmed by the distribution of γ_C^T (Fig. 12, dashed-red line), which is below 0 dB in a quarter of all cases and has the median value of around 2 dB - nearly 6 dB lower than that of γ_D^T. As a result, the peak-cubes of $\mathrm{psSAR_{10g}}$ do not follow the UE location and their distribution is similar to what is observed in absence of the UE.

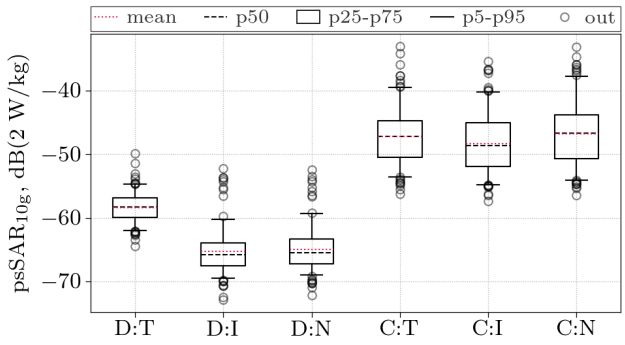

Fig. 14. Distribution parameters of $\mathrm{psSAR_{10g}}$, expressed as a fraction of the ICNIRP general public basic restriction (2 W/kg), induced by $\mathrm{BS_D}$ and $\mathrm{BS_C}$ transmission with the same total power of 1 W. The marker and legend notation is the same as described in Fig. 13.

Interestingly, the collocated BS performs better in the Interferer scenario, having around 1 dB lower median value of γ_C^I (Fig. 12, dashed-green) compared to that of γ_D^I. This can also be seen in the bottom-center of Fig. 11, as a high contrast between the reduced $\bar{E}_{\mathrm{RMS}}$ levels around the UE and the opposite side of the head, where the $\bar{E}_{\mathrm{RMS}}$ maximum is observed (red cross in Fig. 11). However, the reason for this is not an improvement in the interference cancellation, compared to $\mathrm{BS_D}$, but the $\mathrm{BS_C}$ shadowing of the UE by the head. The average value of $\mathbf{G}_C^I$ is around 0 dB (i.e., no $\bar{E}_{\mathrm{RMS}}$ reduction with respect to the non-precoded transmission). This is about 4 dB higher than that of $\mathbf{G}_D^I$ and results in an average SIR of around 7 dB, which is nearly 5 dB below the one for $\mathrm{BS_D}$.

In the Non-user scenario, the mean gain reaches nearly 6 dB, indicating a strong correlation in the channels of the collocated BS: $\bar{E}_{\mathrm{RMS}}$ at a non-user location is significantly increased when the BS targets the UEs that are 5 m away. It is worth noting that the studied multi-user scenario is indeed challenging (by design) for the collocated BS, and a better performance (i.e., higher SIR, more focused E_{RMS}) with the UEs at other positions in the environment could be expected.

3) $\mathrm{psSAR_{10g}}$ with ZF: Fig. 14 shows $\mathrm{SAR_{10g}}$ distributions corresponding to the ZF scenarios shown in Fig. 11 (Rx^+ track as Target, Interferer and Non-user with $\delta = 27$ mm). In the Target scenario, the collocated BS induces more than 11 dB higher $\mathrm{psSAR_{10g}}$ compared to the collocated one. This is in part attributed to the higher absolute peak E_{RMS} values (the locations of which are shown with black crosses in Fig. 11) produced by the $\mathrm{BS_C}$ compared to $\mathrm{BS_D}$.

As mentioned earlier in this section, $\mathrm{BS_D}$ is capable of focusing E_{RMS} producing a 'hot-spot' in the Target scenario. This leads to around 7 dB increase of the induced average $\mathrm{psSAR_{10g}}$ compared to the Interferer and Non-user scenarios (approx. 58 vs. 65 dB below the ICNIRP limit). Even though the average $\mathbf{G}_D^I$ is about 5 dB lower than $\mathbf{G}_D^N$ (see Fig. 13),

the corresponding psSAR_{10g} values are nearly equal. This is explained by the fact that psSAR_{10g} is largely determined by the peak E_{RMS} absolute values and locations in vicinity of the head, which are comparable in these two scenarios. For the same reason, BS_C induces similar average psSAR_{10g} in all three scenarios (-47 ± 1dB, see the three rightmost bars in Fig. 14).

The 95$^{\text{th}}$percentile values of psSAR_{10g} distributions obtained for 1 W total BS power indicate the *realistic worst case* exposure. In the target scenario, BS_D is now more than 15 dB below BS_C, which means that in the infrequent cases of a relatively high psSAR_{10g}, its values are about 40 times lower in the distributed BS configuration compared to the collocated one. For the Non-user scenario this gap increases to nearly 22 dB. This indicates that the environmental DL exposure, i.e. part of the exposure caused by the BS transmission directed towards other users, is almost 160 times lower for BS_D compared to BS_C.

IV. Conclusions

This contribution demonstrated that, considering the human EMF exposure, distributed Massive MIMO deployment has a number of advantages compared to the collocated one. It was shown that in many scenarios, the distributed BS produced a more compact EMF enhancement region around the target receiver using the Maximum Ratio Transmission precoding to maximize the single-user received SNR. This resulted in the lower induced psSAR_{10g} normalized to the incident power density for the distributed BS with two studied normalization approaches. Furthermore, in multi-user scenarios with the interference-canceling Zero-Forcing transmission, the distributed BS induced consistently lower EMF around non-users (relative to the active user equipment). Overall, the realistic worst case exposure of active users and non-users to the distributed Massive MIMO was found to be at lease one and two orders of magnitude lower, respectively, compared to its collocated counterpart.

One possible pathway for advancing the exposure analysis is the inclusion of the network performance indicators (e.g., total throughput, bit error rate) into the model. Another interesting aspect to investigate is the influence of the UE antenna design on the hot-spot shape and size. A more comprehensive study involving a diverse range of the multiplexed UEs' types, locations, and counts in an enhanced network model is the focus of the future research.

Acknowledgements

Sergei Shikhantsov is a postdoctoral fellow of the Special Research Fund (BOF). Arno Thielens is a postdoctoral fellow of the Research Foundation Flanders (FWO) under grant agreement no. 1283921N. This work was supported by ERC through ATTO:A New Concept for Ultrahigh Capacity Wireless Networks under Grant 695495 and Methusalem SHAPE: Next Generation Wireless Networks.

‘

References

[1] T. L. Marzetta, "Noncooperative cellular wireless with unlimited numbers of base station antennas," *IEEE Transactions on Wireless Communications*, vol. 9, no. 11, pp. 3590–3600, 2010.

[2] I. Rahman, S. Modarres Razavi, O. Liberg, C. Hoymann, H. Wiemann, C. Tidestav, P. Schliwa-Bertling, P. Persson, and D. Gerstenberger. 5g evolution toward 5g advanced: An overview of 3gpp releases 17 and 18. [Online]. Available: https://www.ericsson.com/en/reports-and-papers/ericsson-technology-review/articles/5g-evolution-toward-5g-advanced

[3] P. Harris, S. Zhang, M. Beach, E. Mellios, A. Nix, S. Armour, A. Doufexi, K. Nieman, and N. Kundargi, "Los throughput measurements in real-time with a 128-antenna massive mimo testbed," in *2016 IEEE Global Communications Conference (GLOBECOM)*. IEEE, 2016, pp. 1–7.

[4] H. Q. Ngo, E. G. Larsson, and T. L. Marzetta, "Aspects of favorable propagation in massive mimo," in *2014 22nd European Signal Processing Conference (EUSIPCO)*, 2014, pp. 76–80.

[5] X. Wu, N. C. Beaulieu, and D. Liu, "On favorable propagation in massive MIMO systems and different antenna configurations," *IEEE Access*, vol. 5, pp. 5578–5593, 2017.

[6] A. Ashikhmin and T. Marzetta, "Pilot contamination precoding in multi-cell large scale antenna systems," in *2012 IEEE International symposium on information theory proceedings*. IEEE, 2012, pp. 1137–1141.

[7] E. Björnson, E. G. Larsson, and T. L. Marzetta, "Massive MIMO: Ten myths and one critical question," *IEEE Communications Magazine*, vol. 54, no. 2, pp. 114–123, 2016.

[8] U. Madhow, D. R. Brown, S. Dasgupta, and R. Mudumbai, "Distributed massive mimo: Algorithms, architectures and concept systems," in *2014 Information Theory and Applications Workshop (ITA)*. IEEE, 2014, pp. 1–7.

[9] J. Zhang, E. Bjrnson, M. Matthaiou, D. W. K. Ng, H. Yang, and D. J. Love, "Prospective multiple antenna technologies for beyond 5g," *IEEE Journal on Selected Areas in Communications*, vol. 38, no. 8, pp. 1637–1660, 2020.

[10] H. Q. Ngo, A. Ashikhmin, H. Yang, E. G. Larsson, and T. L. Marzetta, "Cell-free massive mimo: Uniformly great service for everyone," in *2015 IEEE 16th international workshop on signal processing advances in wireless communications (SPAWC)*. IEEE, 2015, pp. 201–205.

[11] Z. Chen and E. Bjrnson, "Channel hardening and favorable propagation in cell-free massive mimo with stochastic geometry," *IEEE Transactions on Communications*, vol. 66, no. 11, pp. 5205–5219, 2018.

[12] J. Hederen and P. Frenger, "Improved antenna arrangement for distributed massive mimo," Patent, Dec. 17, 2020, uS Patent App. 16/764,126.

[13] G. Interdonato, E. Björnson, H. Q. Ngo, P. Frenger, and E. G. Larsson, "Ubiquitous cell-free massive mimo communications," *EURASIP Journal on Wireless Communications and Networking*, vol. 2019, no. 1, pp. 1–13, 2019.

[14] E. Björnson, L. Sanguinetti, H. Wymeersch, J. Hoydis, and T. L. Marzetta, "Massive MIMO is a reality-what is next?: Five promising research directions for antenna arrays," *Digital Signal Processing*, vol. 94, pp. 3 – 20, 2019, special Issue on Source Localization in Massive MIMO.

[15] L. Chiaraviglio, C. Lodovisi, S. Bartoletti, A. Elzanaty, and M.-S. Alouini, "Dominance of smartphone exposure in 5g mobile networks," *arXiv preprint arXiv:2211.01077*, 2022.

[16] M. Nedelcu, V. Niu, and T. Petrescu, "Uplink power levels of user equipment in commercial 4g and 5g networks," in *2021 13th International Conference on Electronics, Computers and Artificial Intelligence (ECAI)*, 2021, pp. 1–4.

[17] G. Durgin, N. Patwari, and T. S. Rappaport, "An advanced 3d ray launching method for wireless propagation prediction," in *Vehicular Technology Conference, 1997, IEEE 47th*, vol. 2. IEEE, 1997, pp. 785–789.

[18] G. Spencer and M. Murty, "General ray-tracing procedure," *JOSA*, vol. 52, no. 6, pp. 672–678, 1962.

[19] REMCOM, *Wireless InSite 3.2.0 Reference Manual*, 2017. [Online]. Available: http://www.remcom.com/WirelessInSite

[20] S. Shikhantsov, A. Guevara, A. Thielens, G. Vermeeren, P. Demeester, L. Martens, G. Torfs, S. Pollin, and W. Joseph, "Spatial correlation in indoor massive mimo: Measurements and ray-tracing," *IEEE Antennas and Wireless Propagation Letters*, 2021.

[21] M. Velghe, S. Shikhantsov, L. Martens, W. Joseph, and A. Thielens, "Beam width assessment of a linear array for mamimo applications at 3.5 ghz using measurements and raytracing," in *2020 XXXIIIrd General Assembly and Scientific Symposium of the International Union of Radio Science, 29 August - 5 September 2020*. IEEE, pp. 1–2.

[22] S. Shikhantsov, A. Thielens, G. Vermeeren, E. Tanghe, P. Demeester, L. Martens, G. Torfs, and W. Joseph, "Hybrid ray-tracing/fdtd method for human exposure evaluation of a massive mimo technology in an industrial indoor environment," *IEEE Access*, vol. 7, pp. 21 020–21 031, 2019.

[23] S. Shikhantsov, A. Thielens, G. Vermeeren, E. Tanghe, P. Demeester, G. Torfs, L. Martens, and W. Joseph, "User and non-user EMF-exposure assessment of massive MIMO in an outdoor urban environment using ray-tracing method with stochastic geometry," in *Joint Annual Meeting of the Bioelectromagnetics Society and the European BioElectromagnetics Association (BioEM 2020)*, 2020, pp. 352–355.

[24] G. E. Athanasiadou and A. R. Nix, "Investigation into the sensitivity of the power predictions of a microcellular ray tracing propagation model," *IEEE transactions on Vehicular Technology*, vol. 49, no. 4, pp. 1140–1151, 2000.

[25] S. Shikhantsov, A. Thielens, G. Vermeeren, P. Demeester, L. Martens, G. Torfs, and W. Joseph, "Massive mimo propagation modeling with user-induced coupling effects using ray-tracing and fdtd," *IEEE Journal on Selected Areas in Communications*, vol. 38, no. 9, pp. 1955–1963, 2020.

[26] M.-C. Gosselin, E. Neufeld, H. Moser, E. Huber, S. Farcito, L. Gerber, M. Jedensjö, I. Hilber, F. Di Gennaro, B. Lloyd *et al.*, "Development of a new generation of high-resolution anatomical models for medical device evaluation: the virtual population 3.0," *Physics in medicine and biology*, vol. 59, no. 18, p. 5287, 2014.

[27] J. R. Baumgardner and P. O. Frederickson, "Icosahedral discretization of the two-sphere," *SIAM Journal on Numerical Analysis*, vol. 22, no. 6, pp. 1107–1115, 1985.

[28] T. L. Marzetta, E. G. Larsson, H. Yang, and H. Q. Ngo, *Fundamentals of massive MIMO*. Cambridge University Press, 2016.

[29] H. Q. Ngo, "Massive mimo: Fundamentals and system designs," 2015.

[30] I. 62704, "Iec/ieee international standard – determining the peak spatial-average specific absorption rate (sar) in the human body from wireless communications devices, 30 mhz to 6 ghz - part 1: General requirements for using the finite-difference time-domain (fdtd) method for sar calculations," *IEC/IEEE 62704-1:2017*, pp. 1–86, 2017.

[31] International Commission on Non-Ionizing Radiation Protection *et al.*, "Guidelines for limiting exposure to electromagnetic fields (100 khz to 300 ghz)," *Health Physics*, vol. 118, no. 5, pp. 483–524, 2020.

[32] T. Uusitupa, I. Laakso, S. Ilvonen, and K. Nikoskinen, "SAR variation study from 300 to 5000 MHz for 15 voxel models including different postures," *Physics in Medicine & Biology*, vol. 55, no. 4, p. 1157, 2010.

[33] J. Bakker, M. Paulides, A. Christ, N. Kuster, and G. C. van Rhoon, "Assessment of induced sar in children exposed to electromagnetic plane waves between 10 mhz and 5.6 ghz," *Physics in Medicine & Biology*, vol. 55, no. 11, p. 3115, 2010.

[34] J. Bakker, M. Paulides, E. Neufeld, A. Christ, N. Kuster, and G. Van Rhoon, "Children and adults exposed to electromagnetic fields at the icnirp reference levels: theoretical assessment of the induced peak temperature increase," *Physics in Medicine & Biology*, vol. 56, no. 15, p. 4967, 2011.